



Discrete element simulation of the breakage behavior of porous granules utilizing bond models

Sonja Rotter¹ · Maksym Dosta^{2,3} · Alexander Düster¹

Received: 15 December 2022 / Revised: 15 December 2022 / Accepted: 26 April 2023
© The Author(s) 2023

Abstract

In the development of ships, the aspect of collision safety plays a major role. In this paper, the approach to improve the crashworthiness of ships is to fill the already existing double hull with a granular material. For this purpose, the material used is to be investigated numerically. A discrete element approach is applied for this in the paper presented. Since the breakage behavior of the particles is of particular interest, the discrete element method is used together with a bonded particle method. This approach is extended by a model which is able to take into account the micro-cracks occurring in the material and the energy dissipation caused by them. Using this and other models of the bonded particle method, simulations are carried out and compared with corresponding experiments. A particular focus is on uniaxial compression tests with single particles and particle systems. The single-particle tests are used to determine various simulation parameters relevant to individual particles in terms of geometry and material. In addition, the multi-particle tests provide insight into the behavior of several particles, their interaction and dynamics. These simulations can be used to test the extent to which it is possible to represent porous particles and their fracture behavior by numerical means.

Keywords Discrete element method · Bonded particle method · Particle breakage · Micro-cracking

1 Introduction

With the growing number of ships in our oceans, even with modern navigation and radar equipment, it is not possible to prevent collisions altogether. For this reason, there have been several research projects in recent years that have focused on increasing collision safety. A first step in this direction was the introduction of double hulls for oil tankers by the International Maritime Organization in 1996 [1]. In later years, double hulls were also introduced for other types of ships such as bulk carriers. Nevertheless, ship collisions with severe environmental damage have occurred—for example in 2019 between two cargo ships off the coast of Corsica, result-

ing in an oil spill. In addition to collisions between two ships, it is also necessary to consider collisions between ships and offshore wind turbines—due to the growing importance of renewable forms of energy. Especially in coastal areas where wind farms are built close to main traffic routes, there is an increased risk of collisions with turbine towers and supply vessels [2].

In order to further improve the collision safety, various approaches have been pursued. In [3–5], the influence of different internal structures of the double hull are investigated with respect to their energy absorbing capabilities. In [6], another approach to reduce the impact of a collision is studied by changing the design and material of the bulbous bow. If the bow is able to absorb a larger portion of the impact force by crushing or folding, it is possible that the opponent's hull will not be penetrated.

The solutions mentioned so far have the disadvantage that they can only be applied to the production of new ships. However, since most ships are in service for 20 years or more, it would be of great advantage to find ways to increase the collision safety of existing ships. This can be done by filling the double hull of a ship with a crushable granular material [7, 8]. For this approach, different materials such as

✉ Sonja Rotter
sonja.rotter@tuhh.de

¹ Numerical Structural Analysis with Application in Ship Technology (M-10), Hamburg University of Technology, 21073 Hamburg, Germany

² Institute of Solids Process Engineering and Particle Technology (SPE), Hamburg University of Technology, 21073 Hamburg, Germany

³ Boehringer Ingelheim Pharma GmbH & Co Kg., 88400 Biberach an der Riss, Germany

expanded glass and clay were investigated [9], with the result that expanded glass is most suitable for this purpose [10]. The granules were experimentally studied in several tests [11], focusing on the ability to dissipate energy while transferring loads through the material from the outer to the inner hull. In addition, numerical investigations were performed using the discrete element method (DEM). The approach presented in [12–14] is based on a breakage model where the simulated granular material breaks into several small particles [15]. Here, the challenges are mass conservation and a decreasing time step size due to the decreasing particle size. Therefore, this work follows a different DEM approach in which the granule is simulated as an agglomerate of small primary particles connected by solid massless bridges [16]. Since the failure of the solid bridges plays a key role in the breaking behavior of the agglomerate, several failure algorithms are investigated—including a linear-elastic model [16] and a linear-elastic perfectly plastic model [17]. After an in-depth presentation of the granular material in Sect. 2, the DEM approach is discussed in detail—with particular reference to the different failure approaches—in Sect. 3. Following the outline of the numerical method, Sect. 4.1 presents simulations of some experiments carried out by [11] and the influence of different simulation parameters on the breakage of the agglomerates. In Sect. 4.2, special attention is paid to the extent to which the model used can reproduce the behavior of a large number of granules and their interaction under pressure in a uniaxial compression test. The paper is concluded with a brief summary of the results and an outlook on future work.

2 Granular material

For any material considered to fill the double hull of ships, specific requirements have to be fulfilled. Since ships have to be inspected regularly by a classification society, including an examination of the inside of the hull by a surveyor, it is mandatory to ensure that the hull can be emptied. Thus, pumpable materials which can be sucked from the hull are necessary. Moreover, to mitigate the impact on the ecosystem in the case of a collision, the material has to be non-polluting. In order to comply with fire safety requirements, the material has to be incombustible and, for ship stability requirements, it has to be hydrophobic so as not to change its mass and subsequently the ship's center of gravity over time. Lastly, the weight of the granules lessens the maximum payload of the ship and should therefore be as lightweight as possible. A more comprehensive overview of the requirements can be found in [7].

As mentioned in Sect. 1, different materials have been investigated with regard to the aforementioned requirements—showing that expanded glass particles are the most suitable

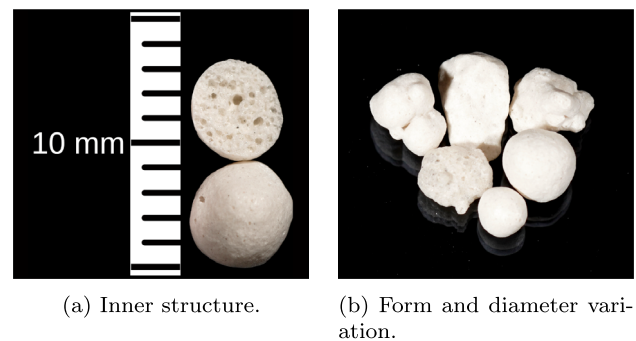


Fig. 1 Porosity and form of Poraver particles

for the given purpose due to their chemical properties [9] and energy dissipation capabilities. One of the glass granules examined in [18] is Poraver expanded glass. Poraver is made of recycled glass bottles and complies with all requirements. With a bulk density of 190 kg/m^3 , [19] it is reasonably light, and the silicate of which the granules are made will reduce to sand if exposed to the ocean. Furthermore, Poraver is already used in industrial applications as a building material, as a carrier and filter material, for fire extinguishing and protection—and as a lightweight crash absorber in the automotive industry.

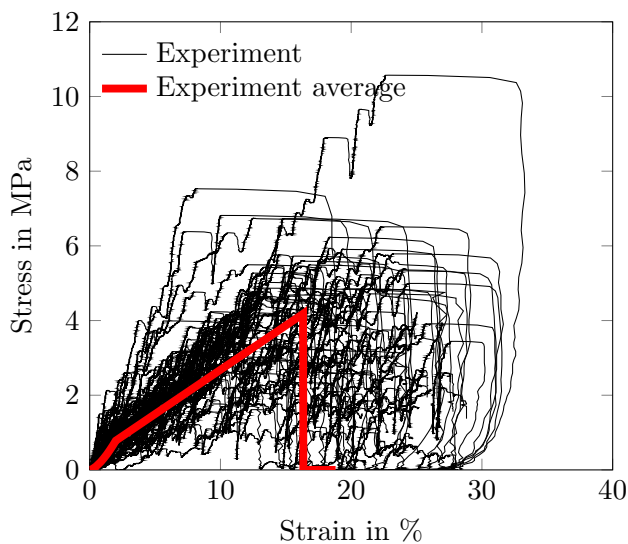
However, the numerical simulation of Poraver presents certain challenges due to the different shapes and the porosity of the individual particles, as a result of the manufacturing process. These differences can be seen in Fig. 1 with regard to the inner structure and the shape and size of the granules. This has considerable influence on the breakage behavior and the effective material parameters. The grain size used for the investigation is 2–4 mm, divided into three diameter fractions in [11] to reduce scatter in the material parameters. Table 1 shows the average material parameters, determined from uniaxial pressure tests, and their standard deviations. Figure 2 shows the stress–strain curves obtained from the same test for the smallest diameter fraction. The test results are shown in black, and the averaged stress–strain curve is depicted in red, clearly demonstrating the large scatter of the test results, despite the subdivision in diameter fractions.

3 Numerical simulation approach

The simulation of breaking particles is quite complex, especially if not only single particles, but also multiple particles are to be considered. It is the micro- or meso-levels that are of interest for single-particle simulations, whereas the macro-level plays a key role for multi-particle interactions. Therefore, the chosen numerical method for this work is the DEM, allowing insight into the micro- as well as the macro-behavior of particles. FEM simulations might be able

Table 1 Granular material parameters describing the crushing (Cr.) behavior [11]

Size range (mm)	Diameter (mm)	Cr. force (N)	Cr. stress (MPa)	Cr. strain (%)	E-Modulus (MPa)	Tests (-)
2.0–2.5	2.16 ± 0.15	14.81 ± 5.19	4.05 ± 1.45	16.49 ± 4.12	564.26 ± 260.60	94
2.5–3.125	2.68 ± 0.18	17.88 ± 5.45	3.19 ± 0.99	16.01 ± 4.98	453.79 ± 158.65	102
3.125–4.0	3.28 ± 0.22	21.62 ± 6.82	2.59 ± 0.87	14.66 ± 4.91	364.84 ± 127.85	106


Fig. 2 Results of the uniaxial pressure test conducted by [11] for a diameter fraction of 2.0–2.5 mm with 94 particles (black) and the average stress–strain curve (red)

to cover the interaction of particles on a macro-level, but they will soon reach their limit when considering breakage. In the case of breakage, even a pure DEM approach like the one introduced by [20] reaches its limitations. In this work, the DEM is therefore combined with a bonded particle method allowing to numerically investigate the breakage of single particles. After introducing the applied simulation approach, the bonded particle method with different breaking criteria will be described.

3.1 Discrete element method

The simulations shown in this paper were performed using the DEM code MUSEN [21]. With the help of this open-source framework, the dynamic behavior of discrete quasi-rigid bodies [22] can be computed. For this purpose, the particle interactions are simulated using a soft-sphere DEM approach [23]. Since each individual particle is simulated, the DEM is computationally very expensive. In order to compute the dynamic behavior of each particle, all interaction partners must be known. Here, Verlet lists [24] are used to determine the interaction partners. They are combined with a linked-cell algorithm [25], which allows to reduce the number of

particles to be considered. This leads to a smaller number of operations and, thus, to a lower computational cost. In addition, this provides the possibility of parallelization, which is performed in MUSEN for both CPUs and GPUs, allowing the simulation of millions of particles in a reasonable time. Once each interaction partner is determined, the resulting contact forces between particles as well as particles and walls are calculated. For this purpose, MUSEN provides a number of different contact models [21], including the well-known Hertz-Mindlin model [26, 27]. This model is suited for calculating the contact forces that occur between Poraver particles. Including these contact forces, Newton's equations of motion

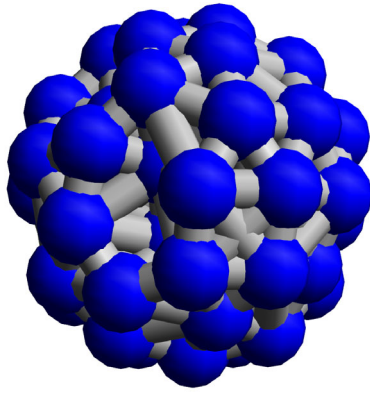
$$m_p \frac{d\mathbf{v}_p}{dt} = \sum_{i=1}^n \mathbf{F}_{p,i} \quad (1)$$

$$I_p \frac{d\boldsymbol{\omega}_p}{dt} = \sum_{i=1}^n \mathbf{M}_{p,i} \quad (2)$$

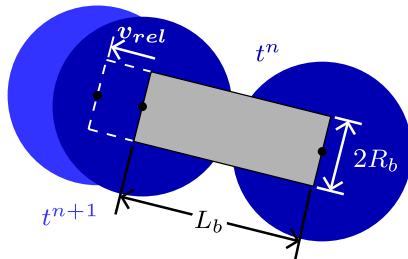
are solved for each particle p . The translation is calculated with Eq. (1) using mass m_p , velocity \mathbf{v}_p , time t , and all forces $\mathbf{F}_{p,i}$ acting on the particle. For the rotation, moment of inertia I_p , rotational velocity $\boldsymbol{\omega}_p$, and all moments $\mathbf{M}_{p,i}$ are needed, leading to Eq. (2). Both equations are solved using an explicit leapfrog scheme [28] for time integration. Using these steps, the momentum generated by external surface or volume forces is propagated through the particle field.

3.2 Bonded particle method

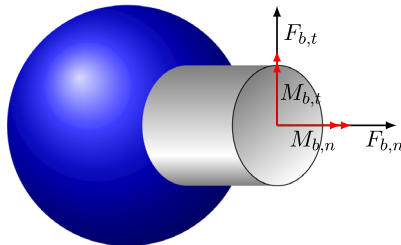
The bonded particle method is based on the approach that particles are modeled as agglomerates consisting of smaller primary particles connected by solid bridges, also called *bonds*. Such an agglomerate can be seen in Fig. 3a with blue primary particles and gray bonds. Please note that not all particles are bonded together, as this depends on the distance between their centers and the maximum allowed initial bond length. This initial length changes over the course of the simulation, depending on the movement of the individual primary particles, as visible in Fig. 3b. Due to this movement, forces and torques occur inside the bonds—which are divided, as illustrated in Fig. 3c, into normal and shear components and are considered to calculate the particles motion with Eqs. (1) and (2).



(a) Primary particles (blue) connected by bonds (grey).



(b) Two primary particles connected by a bond.



(c) Bonded-particle model forces and moments.

Fig. 3 Sketches of the bonded-particle model

In order to simulate Poraver granules, a mesoscale model is used. The necessity of such a mesoscale model arises from the microstructure of the material. Figure 4 shows the inner structure of a Poraver granule as captured by a scanning electron microscope. With a magnification of 67, the structure of the material with large pores embedded in the silicate becomes visible. By further increasing the magnification to 500, it is possible to make out very small pores in-between the larger ones. Due to the scale of these smaller pores, a modeling of the particles on micro-level is not possible, since the diameter of the primary particles would be in the region of nanometers, thus leading to prohibitively small time step sizes and numbers of primary particles. This led to the idea of using a mesoscale model to obtain agglomerates that also take the large pores inside the particles into account, while the influence of the small pores on the breakage behavior has to be covered by the bond model.

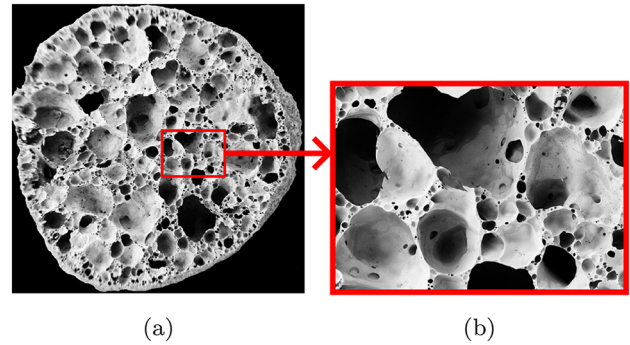


Fig. 4 REM images of a Poraver particle's macrostructure using a magnification of 67 (a) and microstructure using a magnification of 500 (b)

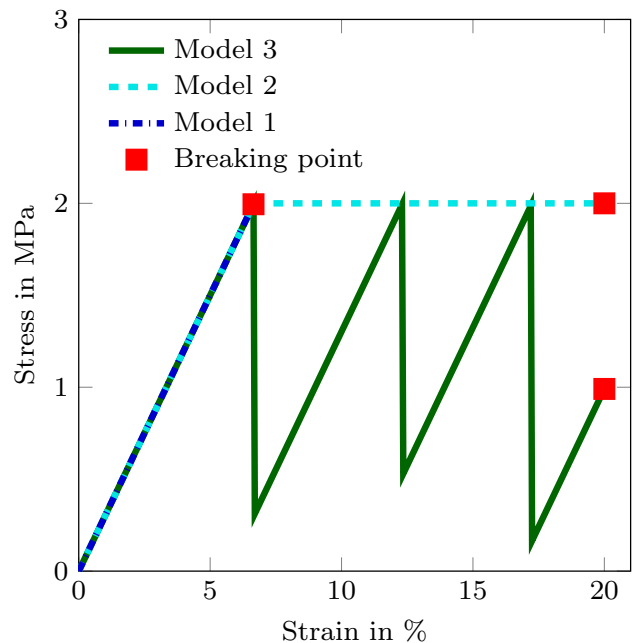


Fig. 5 Stress–strain behavior within one bond for different bond models

With regard to this aspect, different bond models are investigated. It is possible to compute the loads inside the bond in different ways, depending on the material the bond is assumed to represent. Starting from a linear-elastic approach which was introduced by [16] and developed to simulate the breakage of rocks, two more models are implemented to take the plasticity and the micro-cracking of the Poraver material into account. Figure 5 shows the stress–strain curve within a bond subjected to a continuously increasing tension, depending on the model used. The parameters for these curves are chosen to best reveal the differences and similarities.

The three curves all start with a linear stress–strain curve—due to the underlying computation of forces and torques, which is based on beam theory [29]. At each time step, an increment of the resulting force and torque is added

to the current values. These force and torque increments are calculated with

$$\Delta \mathbf{F}_{b,n} = \frac{E_b}{L_b} \cdot A_b \cdot \mathbf{v}_{\text{rel},n} \cdot \Delta t, \quad (3)$$

$$\Delta \mathbf{F}_{b,t} = \frac{E_b}{2L_b(1+\nu)} \cdot A_b \cdot \mathbf{v}_{\text{rel},t} \cdot \Delta t, \quad (4)$$

$$\Delta \mathbf{M}_{b,n} = \frac{-E_b}{2L_b(1+\nu)} \cdot J_b \cdot \boldsymbol{\omega}_{\text{rel},n} \cdot \Delta t, \quad (5)$$

$$\Delta \mathbf{M}_{b,t} = \frac{-E_b}{L_b} \cdot I_b \cdot \boldsymbol{\omega}_{\text{rel},t} \cdot \Delta t, \quad (6)$$

where b indicates that the loads belong to a bond, while n and t stand for normal and tangential direction, respectively. The normal bond force increment $\Delta \mathbf{F}_{b,n}$ is calculated using the bond's Young's modulus E_b and length L_b , the area of the bond's cross section A_b and the relative translational velocity \mathbf{v}_{rel} times the time step Δt . For the tangential bond force increment $\Delta \mathbf{F}_{b,t}$, the Poisson's ratio ν is required as well. Moreover, for normal and tangential torque, the moment of inertia I_b and polar moment of inertia J_b of the bond cross section are needed, respectively, as well as the rotation increment $\Delta \Theta = \boldsymbol{\omega}_{\text{rel}} \cdot \Delta t$, with the relative rotational velocity $\boldsymbol{\omega}_{\text{rel}}$.

The breakage point of the bond for the linear-elastic model, referred to as **Model 1**, is indicated by a red square at the end of the dark blue curve in Fig. 5. The model is described by

$$\sigma_{b,n} = \frac{|\mathbf{F}_{b,n}|}{A_b} + \frac{|\mathbf{M}_{b,t}|}{I_b} \cdot R_b \leq \sigma_{br} \quad (7)$$

and

$$\tau_{b,t} = \frac{|\mathbf{F}_{b,t}|}{A_b} + \frac{|\mathbf{M}_{b,n}|}{J_b} \cdot R_b \leq \tau_{br}, \quad (8)$$

where R_b denotes the bond radius. For this criterion, the bond breaks when the bond's normal stress $\sigma_{b,n}$ exceeds the normal strength σ_{br} or when the shear stress $\tau_{b,t}$ exceeds the tangential strength τ_{br} . This means that the corresponding bond is removed from the discretization, leading to cracks in the agglomerate where the primary particles are no longer connected.

In order to study different modeling approaches, a second model was implemented based on **Model 1**, expanded by a linear-elastic perfect-plastic approach [17], resulting in **Model 2**. For this approach, the maximum stress that can occur in the bond is limited by the yield strength. This means that the bond's total strain

$$\varepsilon_{b,T} = \varepsilon_{b,e} + \varepsilon_{b,p} \quad (9)$$

is composed of an elastic part $\varepsilon_{b,e}$ and a plastic part $\varepsilon_{b,p}$. Thus, the elastic stress in the bond σ_b is

$$\sigma_b = k_b \cdot (\varepsilon_{b,T} - \varepsilon_{b,p}) \quad (10)$$

with the bond's stiffness k_b . Together with the yield stress $\sigma_{b,y}$ of the bond, this leads to the yield condition

$$f(\sigma) |\sigma_b| - \sigma_{b,y} \leq 0 \quad (11)$$

limiting the stress which can occur inside the bond. In Fig. 5, the stress–strain curve for **Model 2** is depicted in cyan. First, the stress increases linearly as for **Model 1**, but the stress remains constant after reaching the yield stress. Finally, when a maximum strain is reached, the bond breaks. This approach takes the plasticity of the material into account, due to occurring micro-cracks.

The third approach is based on a model in which stress drops occur every time the yield stress is reached. This is done by reducing the stress with a probabilistic approach due to the random occurrence of micro-cracks. The approach of the micro-cracking model or **Model 3** is represented by a dark green line in Fig. 5. Again, the stress–strain curve shows a linear increase until the yield stress is reached, followed by a drop in stress. Figure 6 illustrates how cracks in the bond occur under tension.

When a load is applied to the bond, the stress starts to increase, as indicated by **a** in Fig. 7. At this point, the bond is still intact, as can be seen in Fig. 6a. An increase in the applied tension eventually leads to a crack in the bond shown in Fig. 6b, corresponding to a stress drop in Fig. 7, marked with **b**. The stress reduction corresponding to the micro-cracks is calculated by

$$\sigma_{b,\text{rem}} = \eta_W \cdot \sigma_b \quad (12)$$

yielding the remaining stress $\sigma_{b,\text{rem}}$ by multiplying the stress obtained from Eq. (10) with a damage factor η_W , which is randomly distributed uniformly between 0 and 1. After computing the stress reduction in this way, the stress increases linearly again, similar to the initial elastic behavior, until the yield stress is reached once again and another micro-crack appears, see Fig. 6c. The bond's breakage criterion again depends on the bond's strain, so that the bond disappears when

$$\varepsilon_{b,T} > \varepsilon_{b,\text{max}} \quad (13)$$

holds with the maximum bonds strain $\varepsilon_{b,\text{max}}$. At this point, the whole bond is cracked, as shown in Fig. 6d, and the bond is thus removed from the simulation.

In order to investigate the influence of the bond model on the breakage of an agglomerate, simulations were carried out

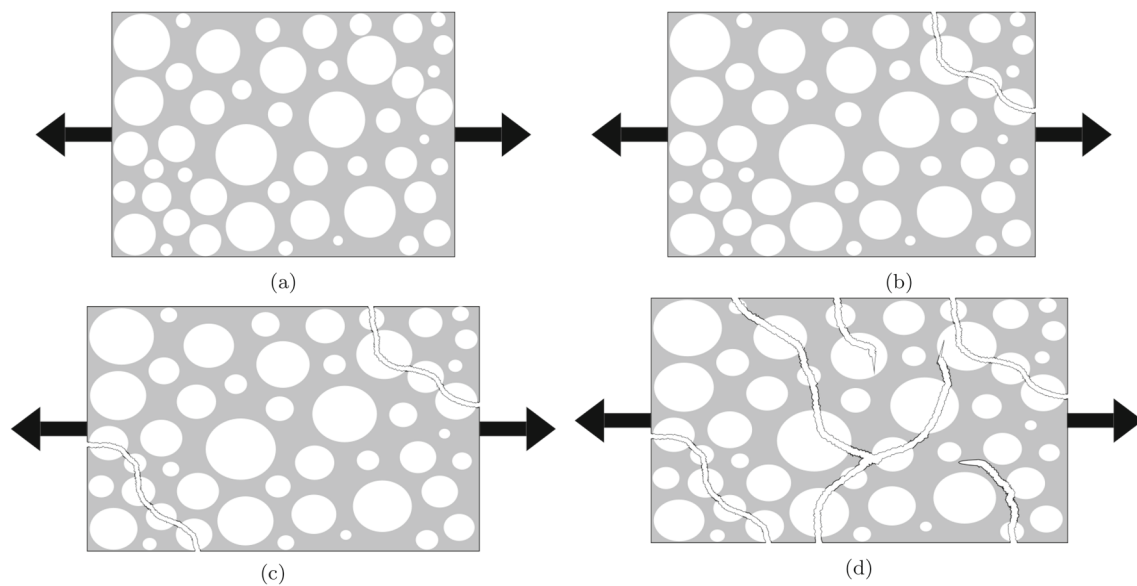


Fig. 6 Schematic representation of the microscale cracking phenomena described with the micro-cracking bond model (**Model 3**)

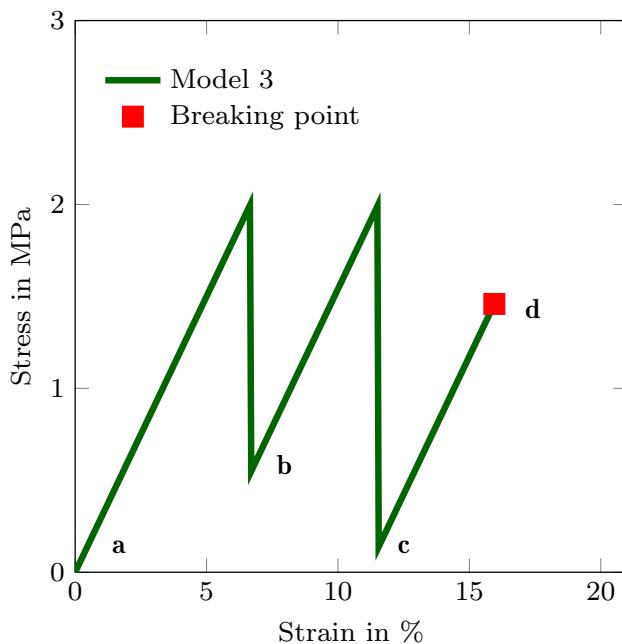


Fig. 7 Stress progression within one bond for **Model 3**

with all three models introduced. The results of these simulations are presented in the following section and compared with the average experimental results from Fig. 2.

4 Uniaxial compression tests

Uniaxial compression tests for single- and multiple particles are particularly suitable for investigating the material param-

eters of granules. Compression tests can be used to investigate the stress–strain behavior as well as the breakage of single particles and particle collectives, their Young’s modulus, and the crushing strength.

4.1 Single particle tests

For single-particle tests carried out with a *Texture Analyzer TA.XTPlus*, see Fig. 8, individual Poraver grains are placed on a metal plate and crushed by a metal stamp with a constant velocity v_0 of $50 \mu\text{m/s}$, as depicted in the upper right corner in Fig. 8. The resulting stress–strain curves are averaged and used as a reference for single-particle simulations. First, single-particle simulations are performed with a spherical agglomerate consisting of 361 primary particles with a diameter of 0.25 mm and 2159 bonds with identical diameters. To ensure equal initial conditions for the comparison of the bond models, the same agglomerate is used in each simulation, applying the material parameters listed in Table 2.

For these first simulations, the average values gained from the experiments are used for the crushing strength and the Young’s modulus. The yield stress and breakage strain are chosen such that the simulations yield reasonable results. To reduce computation time, a compression velocity of 10 mm/s is used in all three simulations. The influence of the compression velocity on the outcome of the simulation is investigated, in addition to several other simulation parameters, as will be discussed later on.

Figure 9 shows the results of uniaxial compression test simulations with all three described bond models compared to the averaged experimental results. In addition, the bonds fracture ratio is plotted which indicates the percentage of

Table 2 Simulation parameters for bond model comparison

Model	Cr. strength (MPa)	Yield stress (MPa)	E-Modulus (MPa)	breakage strain (mm)
1	4.05	2	564.26	
2	4.05	2	564.26	0.0075
3	4.05	2	564.26	0.0075

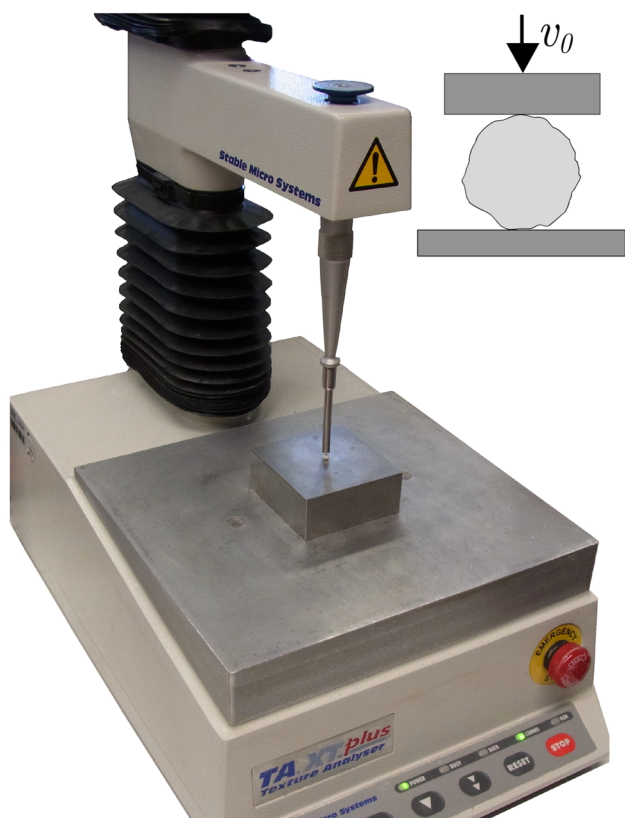


Fig. 8 Experimental uniaxial compression test set up

destroyed bonds. In particular, the difference between the fully linear elastic model and the two plastic models is visible. Due to the breakage criterion of **Model 1**, a large number of bonds are removed simultaneously from the simulation, leading to stress drops represented by the dark blue line. Furthermore, **Model 1** leads to a steeper stress–strain curve than the other two models which differs more from the average experimental results. **Model 2** and **3** are very similar, and due to the strain-based breakage criterion, the peak stress is smaller than for **Model 1** since the crushing strength is higher than the yield strength. Moreover the stress drops for **Model 2** and **3** are much less severe. This leads to a quite similar slope of the stress–strain curve of **Model 2** compared to the experiments. The consideration of the micro-cracks through **Model 3** yields even the same gradient as compared to the experiment. From the comparison, it turns out that **Model 3** is best suited for the simulation of Poraver particles and

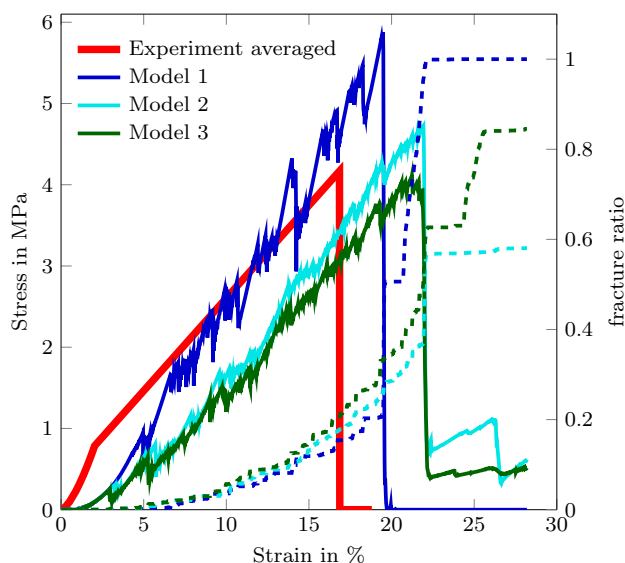


Fig. 9 Results of uniaxial pressure test simulations with all three bond models compared to average experimental results

will therefore be used for all following single agglomerate compression test simulations.

4.1.1 Global simulations parameters

Due to the use of agglomerates consisting of small primary particles and bonds in combination with an explicit time integration scheme, there are certain limitations regarding the appropriate time step size. The critical time step size for the presented simulations is dependent on two factors. On the one hand, it depends on particle–particle contact—which is calculated using the Rayleigh time step size $\Delta t_{\text{Rayleigh}}$ —and on the other hand on the critical time step size for bonded contacts Δt_{bond} [30]. Therefore, the simulation time step is taken as 10% of the critical value [31]:

$$\Delta t_{\text{rec}} = 0.1 \cdot \min (\Delta t_{\text{Rayleigh}}, \Delta t_{\text{bond}}) \tag{14}$$

The Rayleigh time step is calculated with regard to the primary particles’ radius r_p and density ρ_p as well as their shear modulus G_p and Poisson’s ratio ν_p with

$$\Delta t_{\text{Rayleigh}} = \frac{\pi r_p \sqrt{\left(\frac{\rho_p}{G_p}\right)}}{0.1631 \nu_p + 0.8766} \tag{15}$$

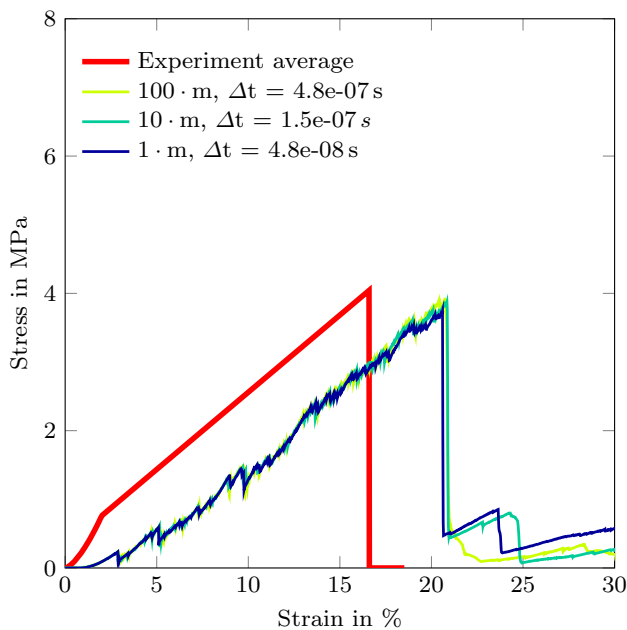


Fig. 10 Influence of mass scaling on the simulation results

The critical time step size for the bonded contact Δt_{bond} is computed as

$$\Delta t_{\text{bond}} = 2 \sqrt{\frac{m_{p,\text{min}}}{K_{b,\text{max}}}} \quad (16)$$

depending on the minimal particle mass $m_{p,\text{min}}$ and the maximum bond stiffness component

$$K_{b,\text{max}} = \max \left(\frac{E_b \cdot A_b}{L_{b,\text{init}}}, \frac{E_b \cdot A_b}{2 \cdot L_{b,\text{init}} \cdot (1 + \nu_b)} \right) \quad (17)$$

with the initial bond length $L_{b,\text{init}}$. Since both time step sizes depend on the primary particle mass or density, respectively, a common way to increase the recommended simulation time step size is **mass scaling** [32]. For this, the material density is increased while the gravity is lowered accordingly. In order to make sure that the mass scaling does not affect the results, simulations with three different mass scalings are compared in Fig. 10. From this, it is evident that the time step size increases with increasing mass, i.e., the higher the mass scaling, the bigger the time step size can be chosen. Moreover, no influence of the scaling on the simulation result is apparent, so that a mass scaling of factor 100 can be used, yielding a time step size increase in a factor of 10.

To further investigate the influence of the **time step size**, it is increased by a factor of 10 several times—starting from a time step size of 5×10^{-10} s, while the mass remains the same. The results of these simulations are presented in Fig. 11. Since the time step size calculated with Eqs. (14) to (17) is only the recommended time step, even simulations with a

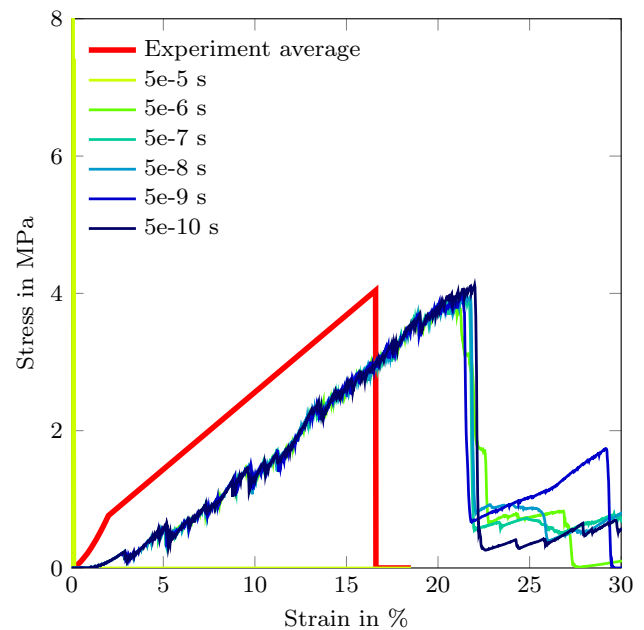


Fig. 11 Influence of the time step size on the simulation results

time step size of 5×10^{-6} s run stable and yield very similar results as simulations with a time step size of 5×10^{-10} s. However, using larger time steps leads to instabilities and a large numerical error. Nevertheless, due to the low dynamics of the experiment and the use of only one agglomerate, it is possible to use a bigger time step than the recommended one.

In addition to the mass scaling and time step size, a third global simulation property is investigated, namely the **compression velocity**. Even with a time step size of 5×10^{-6} , a simulation with a velocity of $50 \mu\text{m/s}$ used in the experiments and thus simulating 12 s of real time, would take about 8 h of computational time. Hence, it is necessary to adapt the compression velocity in order to obtain a reasonable computation time. For this reason, the influence of the compression velocity is investigated in the range from 0.1 to 100 mm/s. As can be seen in Fig. 12, the simulation runs stable and leads to similar results with all tested velocities. However, a crushing velocity of 100 mm/s yields a less pronounced micro-cracking, as can be seen from the less rapid stress changes, especially compared to the results computed with a velocity of 1 mm/s. This is due to the fact that the agglomerate and thus the bonds are deformed to such an extent within one time step that the algorithm presented in Sect. 3.2 does not apply, but the bonds break instantly without prior stress drops. Owing to these results, a velocity of 10 mm/s is used for all further simulations, resulting in a computational time of 5 min, which makes comprehensive parameter studies possible.

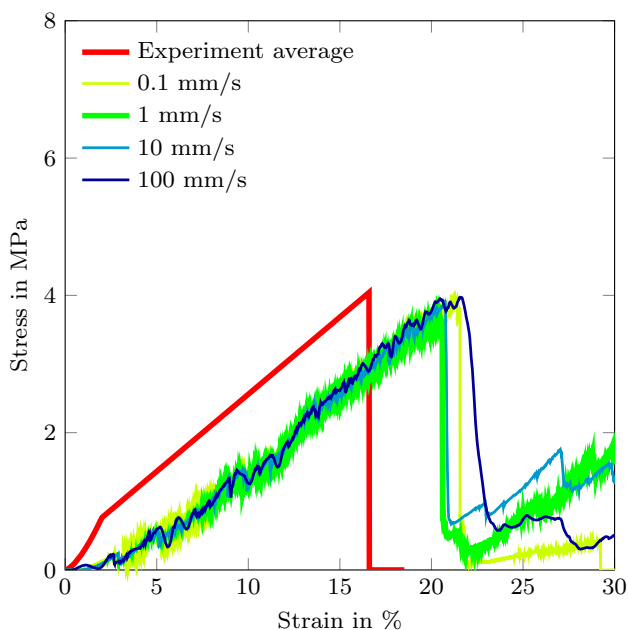


Fig. 12 Influence of the compression velocity on the simulation results

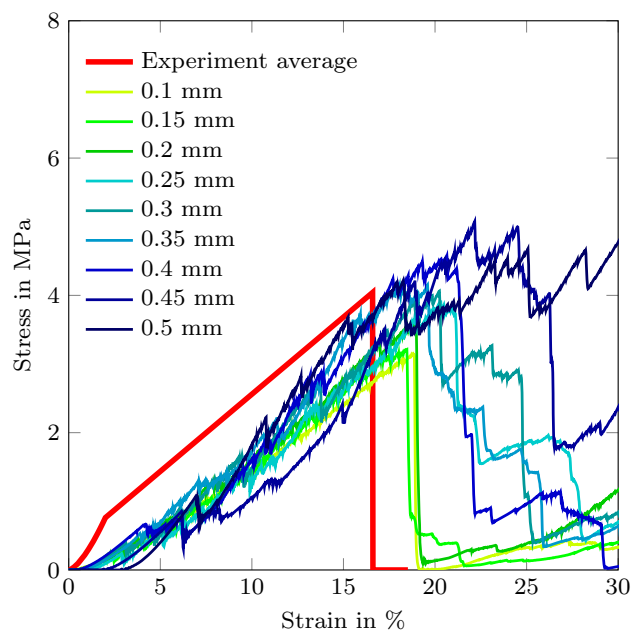


Fig. 14 Influence of the primary particle diameter on the simulation results

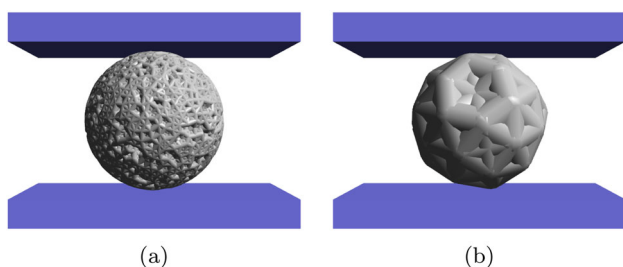


Fig. 13 Variation of primary particle diameter from 0.1 mm (a) to 0.5 mm (b)

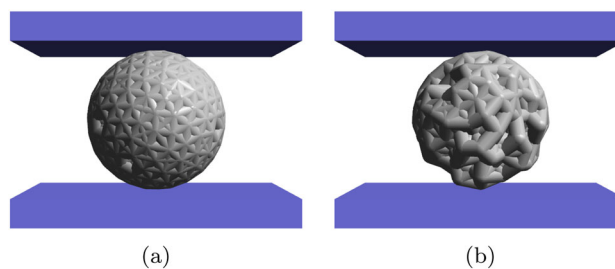


Fig. 15 Variation of agglomerate porosity from 30% (a) to 60% (b)

4.1.2 Geometrical simulation parameters

Having determined the global simulation parameters described above, the main geometrical parameters are investigated. The first parameter to be examined with regard to its influence on the agglomerate's breakage behavior is the **primary particle diameter**. Several simulations are carried out with primary particles of 0.1 mm diameter (Fig. 13a) to 0.5 mm diameter (Fig. 13b) in steps of 0.05 mm.

The resulting stress–strain curves are depicted in Fig. 14. Up to a particle diameter of 0.3 mm, the differences in the curve and thus the influence on the breakage behavior of the agglomerate are negligible. If the primary particle diameter is chosen larger than 0.3 mm, the influence becomes apparent. Since the number of bonds in the agglomerate decreases with an increasing primary particle diameter, the stress drops get more severe if single bonds break. Furthermore, the initial slope of the stress–strain curve is influenced by the number of particles which are initially in contact with the top and

bottom plate. A lack of contact results from the way the primary particles are packed inside the computational volume that represents the volume in which particles can be generated depending on the porosity and form of the resulting agglomerate. In order to minimize these effects, a primary particle diameter of 0.25 mm is chosen for further studies.

The next parameter to be investigated is the packing **porosity of the agglomerate**, which is used to model the macrostructure of the Poraver particles. Since the granule structures and thus also the porosity vary, the aim is to find the porosity that best corresponds to the average stiffness of the particles. For this purpose, porosities between 30 and 60% are investigated. Figure 15a shows an agglomerate with a porosity of 30%, which, as can be seen, leads to a dense packing. In contrast, a porosity of 60% results in a highly porous particle, as shown in Fig. 15b. Since the bonds are considered to be massless, only the primary particles are taken into account in the definition of the porosity.

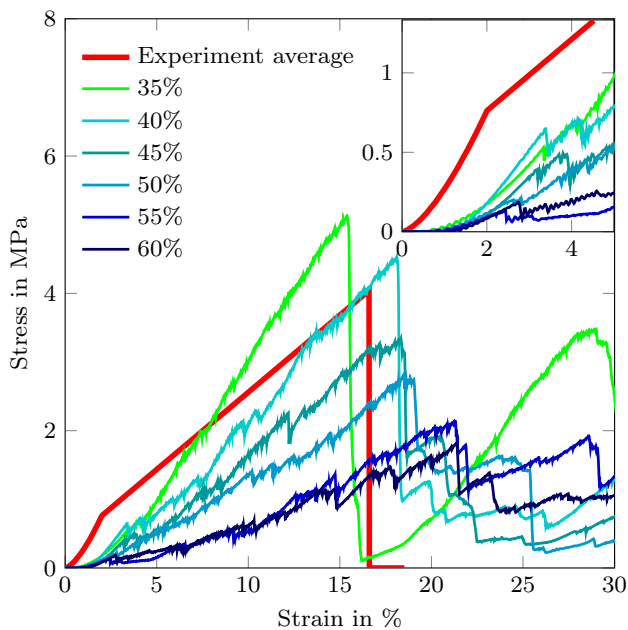


Fig. 16 Influence of the agglomerate porosity on the simulation results

The corresponding stress–strain curves are illustrated in Fig. 16.

The influence of the agglomerate porosity is clearly visible. The denser the packing, the stiffer the agglomerate gets. In the case of 30%, the unphysical inter-particle overlaps and inner stresses become too large. Thereafter, with an increasing porosity, the breakage strain increases, while the breakage stress decreases, corresponding to a decrease in the agglomerate’s stiffness. However, the porosity seems to have only little influence on the initial stiffness. With a porosity of 45%, the slope of the stress–strain curve determined from the simulation equals the slope of the average experimental results.

Since the Poraver particles are mostly slightly elliptical instead of fully spherical, one parameter to be investigated is the **agglomerate’s shape**. To get an elliptical form, the diameter of the analytical volume, shown in light green in Fig. 17, is slightly increased from 2.16 mm diameter to 2.36 mm diameter. To ensure an elliptical or flattened shape, the particle generation is restricted from placing particles in real geometries, like the top and bottom plate, shown in purple. Figure 17 shows a spherical agglomerate on the left-hand side and a flattened one on the right-hand side. As the diameter of the particles used in the experiment is measured between the bottom plate and the stamp, the increase in the diameter of the analytical volume has no influence on the comparability.

In addition, Fig. 18 depicts the influence of this flattening, which results from the enlargement of the diameter of the analytical volume. Due to the number of agglomerates that are initially in contact with the upper plate, increasing with

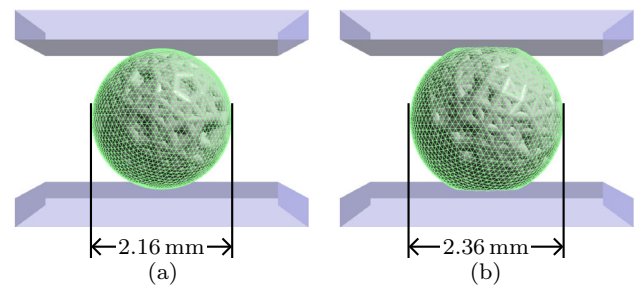


Fig. 17 Variation of agglomerate shape from spherical (a) to flattened (b)

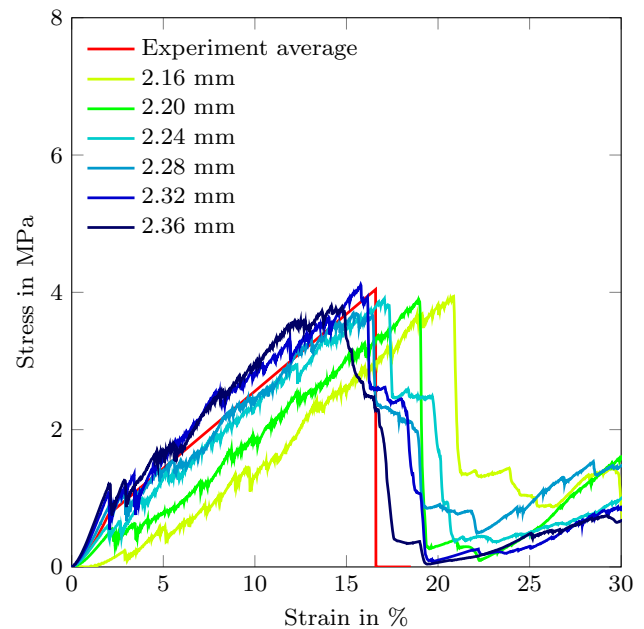


Fig. 18 Influence of the agglomerate shape on the simulation results

an extended flattening of the agglomerate, the initial stiffness and thus the agglomerate’s Young’s modulus increases. Moreover, the slope of the remaining curve is equal for all states of flattening, and the crushing strength is the same as well. However, the crushing strain decreases slightly with an increasing flattening of the agglomerate. This leads to the conclusion that the shape of the agglomerate has considerable influence on its Young’s modulus, without strongly influencing its overall breaking behavior. Thus, the shape has the opposite effect on the breakage of the agglomerate as the porosity. Together, these parameters give the opportunity to influence the outcome of the simulation significantly, and they can be used to generate an optimized agglomerate.

4.1.3 Material parameters

After studying the influence of geometrical parameters on the simulation results, the material parameters of the primary particles and bonds are investigated. In order to make

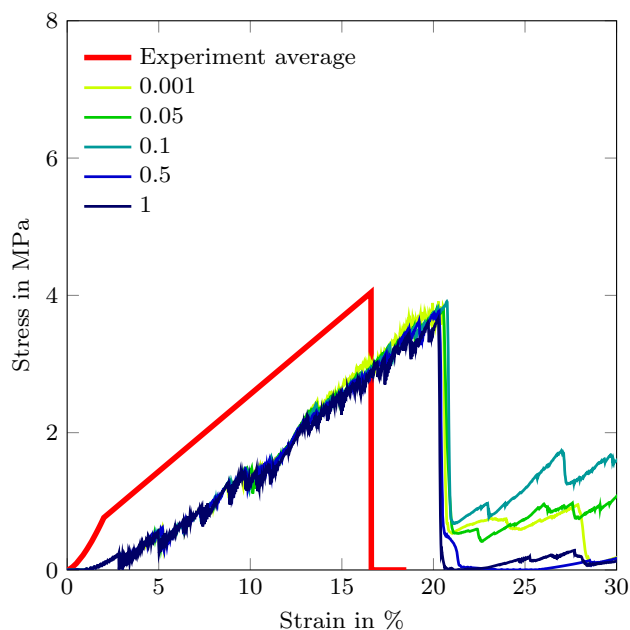


Fig. 19 Influence of the restitution coefficient on the simulation results

sure that rearranged primary particles have no influence on the outcomes of the study, each simulation investigating the material properties is carried out with the same agglomerate. The first of the material parameters to be investigated is the **restitution coefficient**, which influences the energy dissipation during impact [33]. The restitution coefficient is therefore varied between 0 and 1 in several steps, which can be gained from Fig. 19. A coefficient of 1 indicates thereby a fully elastic contact, while 0 leads to a fully plastic contact [34]. However, as can be seen in Fig. 19, the restitution coefficient has no influence on the resulting stress–strain curve. This is due to the fact that the considered simulation is not highly dynamic. If it were, the restitution coefficient would play a much more important role.

Apart from the coefficient of restitution, the **Young's modulus** of the primary particle and the bond are investigated regarding their influence on the simulation results. Since the simulations are based on agglomerates instead of single particles to represent individual grains,

it is not to be expected that material properties gained by experiments can be directly used in the simulation. Due to the structure of the agglomerates, consisting of primary particles and bonds, parameter studies have to be carried out in order to find suitable properties which lead to simulation results comparable to the breakage behavior observed in the experiments. To explore the influence of the Young's modulus on the stress–strain curve, the Young's moduli for the primary particle and the bond are varied from 100 to 1000 MPa in steps of 100 MPa. Figure 20 shows a selection of the simulation results for the changes in the primary particle's Young's

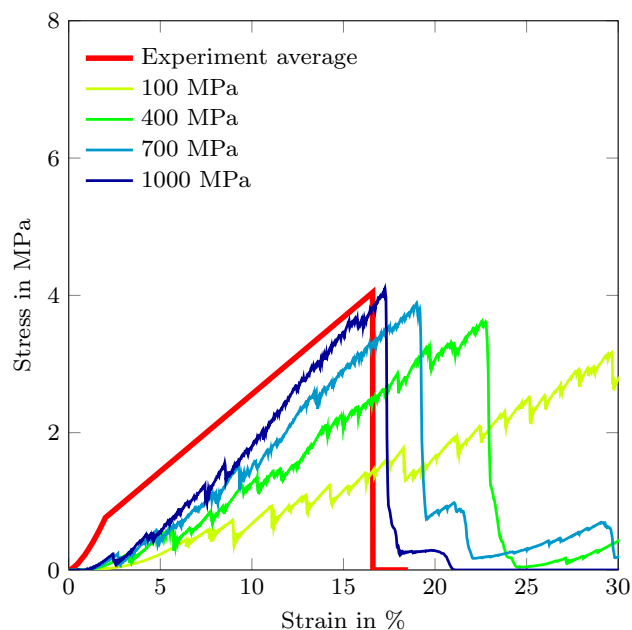


Fig. 20 Influence of the primary particle's Young's modulus on the simulation results

modulus. While the crushing strength remains almost the same for all values, the crushing strain decreases with an increasing Young's modulus.

In contrast to this, the influence of the bond's Young's modulus is much less significant, as can be seen in Fig. 21. Down to a value of 100 MPa, a decrease in the property leads to a slight decrease in crushing strength and strain. However, for 100 MPa, the agglomerate is not as resistant as for larger Young's moduli.

Due to the used bond model, the bond's **yield stress** is investigated instead of its crushing strength. As can be seen in Fig. 22, an increase in the bond's yield stress leads to an increase in the agglomerate's crushing stress and strain. This corresponds to the micro-cracking bond model introduced in Sect. 3.2. With an increased yield stress, the bonds are able to carry larger amounts of stress before micro-cracks occur, reducing the stress in the agglomerate.

4.1.4 Optimized agglomerate

Based on the presented studies, a design of experiment approach is used to generate a set of parameters yielding an improved agglomerate for a diameter fraction of 2.0–2.5 mm. The agglomerate's height is set to 2.16 mm, which is equivalent to the average particle diameter of the considered fraction, see Table 1. In order to generate a slight flattening, the diameter of the analysis volume is set to 2.3 mm. The agglomerate has a porosity of 45%, and the material properties are set to 420 MPa for the Young's modulus of the primary particles and bonds—and 5.6 MPa for the

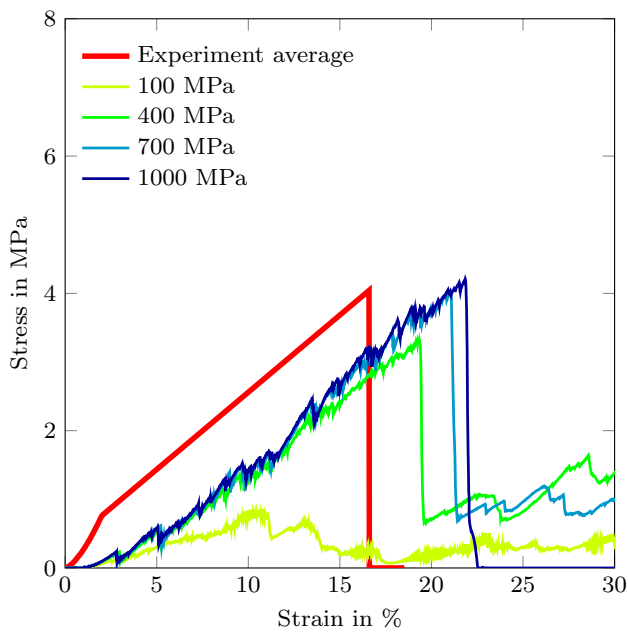


Fig. 21 Influence of the bond's Young's modulus on the simulation results

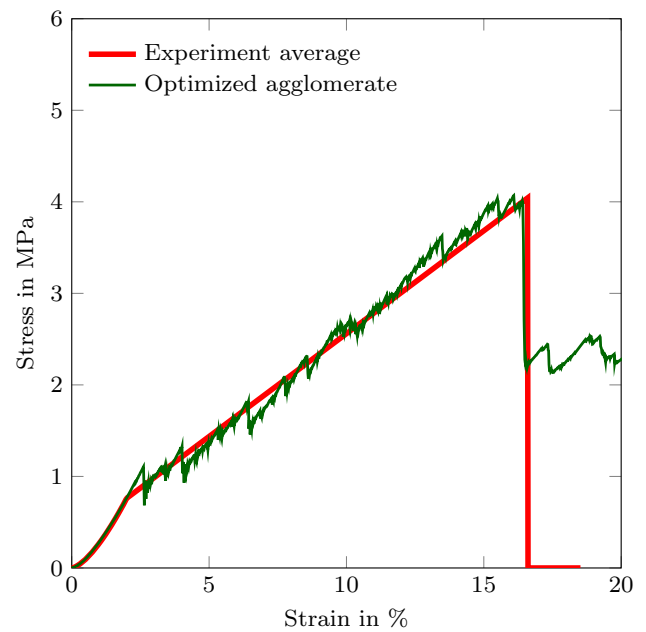


Fig. 23 Simulation results of an optimized agglomerate

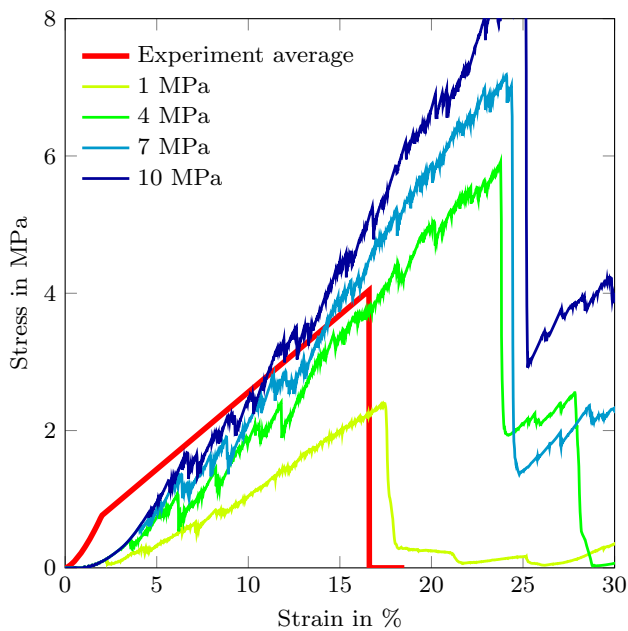


Fig. 22 Influence of the bond's yield stress on the simulation results

bond's yield stress. The resulting stress–strain curve is shown in Fig. 23. These findings are used for further simulations.

4.2 Multi-particle tests

In addition to the single-particle pressure tests, multi-particle compression tests, also known as oedometer tests, were carried out. The experimental setup is shown in Fig. 24.

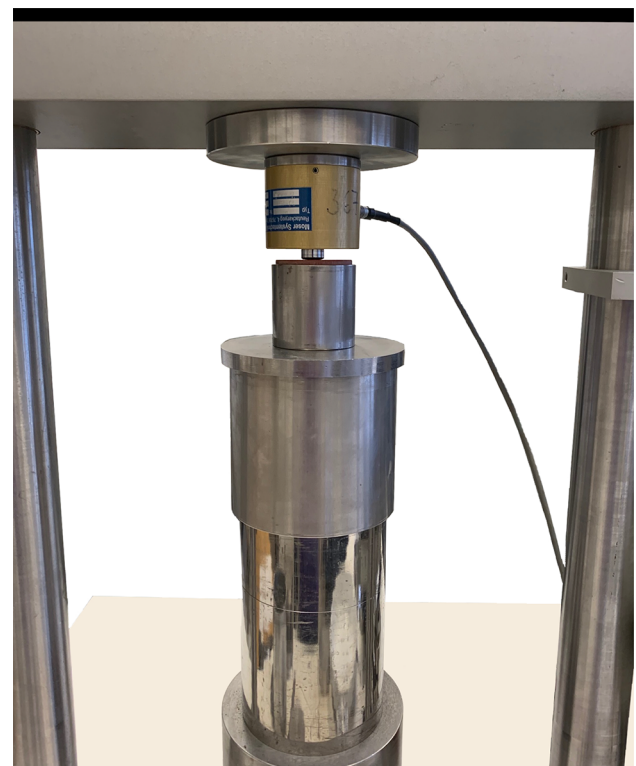


Fig. 24 Experimental oedometer setup

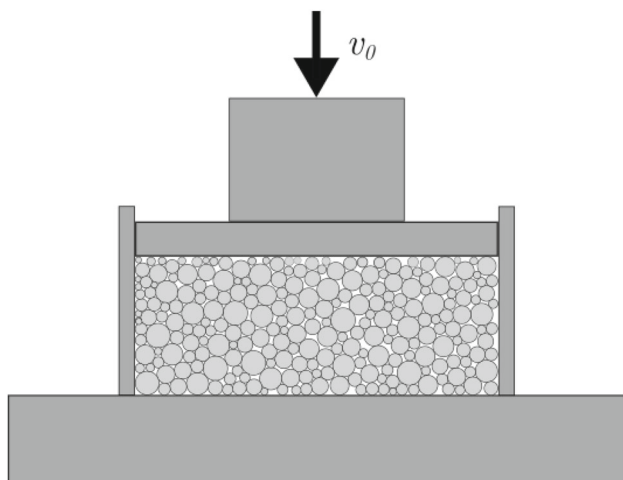


Fig. 25 Oedometer test setup sketch

In this test, a steel cylinder is filled with a certain amount of Poraver particles—which are then compressed by moving a cylindrical plate downward with a velocity $v_0 = 1 \text{ mm/min}$, as shown in Fig. 25. Oedometer tests give a good insight into the interaction of particles under pressure and, thus, a better idea of the behavior of the particles in a double hull during a collision.

In order to achieve the best possible initial conditions for the simulation, the experimental setup is recreated in the model. A cylinder with an inner diameter of 50 mm is filled up to a height of 19.2 mm—with 1396 agglomerates that have a weight of 7.1 g. Moreover, agglomerates from all three diameter fractions are used to represent the parameter scattering. The number of agglomerates from the respective fractions was optimized on the basis of the total number of particles, their weight, and the filling height. After recreating the experiment, the same setup is used for different simulations. However, since the velocity used in the experiments leads to a duration of 10 min, a simulation velocity of 100 mm/s is used to be able to simulate the oedometer test in an acceptable time. Moreover, also in order to reduce computational time, the number of primary particles is set to 200 in each agglomerate—leading to a total number of 299 200 primary particles and 1 704 537 bonds. In order to illustrate the necessity of modeling the crushing of particles, the simulation is also carried out without the breakage, see Fig. 26

Figure 27 shows the resulting stress–strain curves of the simulations accounting for breakage in comparison to the experimental results. All three models underestimate the stiffness of the particles at the beginning of the compression. **Model 1** results in a nearly linear increase in stress, intersecting the experimental results at around 13% strain. The resulting curves gained with **Model 2** and **3** are very similar, running below the experimental curve up to a strain

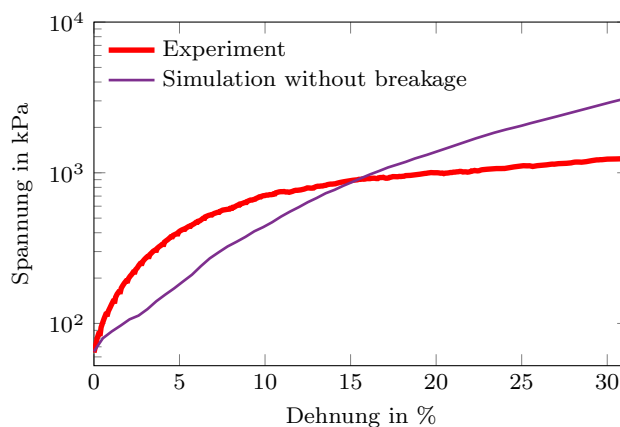


Fig. 26 Oedometer test simulation without breakage of agglomerates

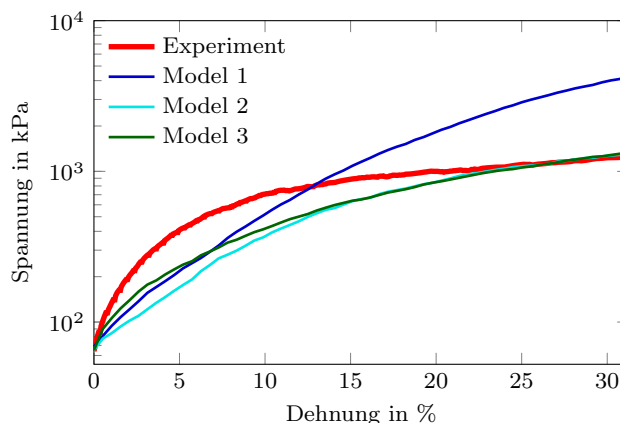


Fig. 27 Oedometer test simulations with all three bond models

of 27%. **Model 3** leads to a slightly stiffer behavior in the initial state of the simulation compared to **Model 2**. At around 15% strain, the curves resulting from the simulations with **Model 2** and **3** meet, and they are very similar from this point onward. Overall, **Model 3** gives a fairly good result. However, the initial stiffness is not yet covered by either of the models.

Therefore, additional simulations are carried out with different friction coefficients [35]. The initial curve is simulated with default parameters of 0.05 for sliding and rolling friction between the particles and particle and wall, indicated as Friction 1, just to exclude the influence of the friction and get a clear result governed by the influence of the model. The second friction parameter set (Friction 2) is gained from experimental results presented in [9] and bulk test simulations—leading to a sliding friction of 0.87 and a rolling friction of 0.1 for particle interactions and a differing sliding friction of 0.48 for particle-wall contact. As can be seen in Fig. 28, this parameter set overestimates the stiffness of the interacting particles. This is due to the coarse representation of the agglomerates, which leads to interlocking between primary particles of different agglomerates. There-

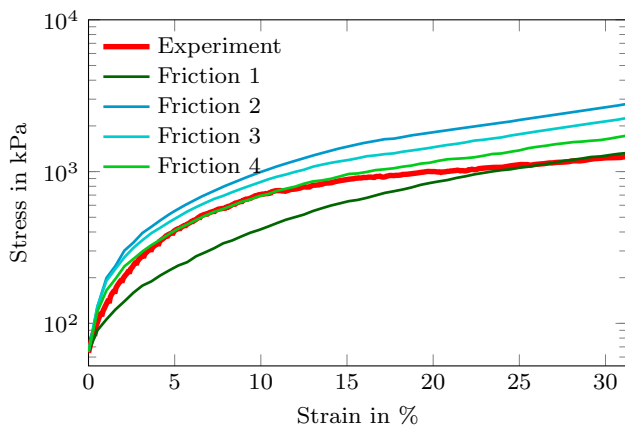


Fig. 28 Oedometer test simulations with different friction coefficients

fore, it is necessary to adjust friction and, thus, two more sliding friction values for particle interactions are tested. For the simulations denoted with Friction 3, a sliding friction of 0.4 is used, while the rolling friction remains at 0.1—and the same holds for Friction 4 with a sliding friction of 0.2. Up to a strain of 15%, Friction 4 leads to a very good agreement with the experimental results. However, since primary particles cannot break, the relatively coarse representation of the agglomerates leads to the situation that the stiffness for larger strains is overestimated.

Even though the results are already quite good, more simulations with smaller primary particles as well as several parameter studies should be carried out to get a deeper understanding of multi-particle interactions. This includes, for example, the crushing velocity. Even if single-particle tests show no influence of the crushing velocity on the simulation results, this does not necessarily apply to multi-particle tests.

5 Conclusion

The aim of this work was to simulate the breakage of a granular material. Therefore, single grains were modeled as agglomerates consisting of primary particles and bonds. Based on this, it was possible to develop and investigate a bonded particle model that is capable of simulating the breakage of porous granules. To this purpose, a linear-elastic perfect-plastic model was extended by a micro-cracking approach. These micro-cracks are modeled with stress drops that occur each time the bond's yield stress is reached. This and two other models were used to simulate single- and multi-particle compression tests. These simulations showed a good agreement of the simulation results with the micro-cracking model compared to the experiments. Moreover, several simulation parameters were investigated with regard to their influence on the breakage behavior of the tested agglom-

erates. These studies show that mass scaling (which gives the opportunity of using bigger time steps) and the compression velocity have no significant influence on the simulation result. Even the time-step size is not bound to the usual recommendations for DEM simulations for single-particle compression tests. The simulation only fails if the time step size is considerably larger than the calculated maximum time step. Regarding the geometrical parameters, the agglomerate's porosity and shape are the most influential factors. The agglomerate's shape has a significant influence on the initial stiffness of the agglomerate and thus its Young's modulus. In addition, the investigation of several material parameters shows that the primary particle's Young's modulus and the bond's yield strength have the greatest influence on the agglomerate's breakage. With the help of these findings, it is possible to create an agglomerate whose stress–strain curve fits the average experimental results.

Furthermore, all three bond models were used to simulate a multi-particle compression test. Here, too, the best results were achieved with the newly introduced micro-cracking bond model (**Model 3**). Further numerical investigation revealed that the consideration of friction between particles and particles and the wall play an important role. There is still room for further improvements regarding the agglomerates and the parameters used in the simulations. Nevertheless, the oedometer test shows promising results—and it is a big step toward the general goal of the project, which is to carry out adequate coupled DEM-FEM simulations of collisions with particle-filled double hulls.

For this purpose, in order to gain more insight into multi-particle interactions, new experiments will be carried out with smaller amounts of particles and different crushing velocities. Moreover, sieved samples are going to be tested to investigate the influence of the particle size on the crushing behavior. Smaller amounts of particles in the oedometer tests allow for more extensive parameter studies in simulations, which can be helpful to investigate certain effects in more detail.

Acknowledgements The presented research is funded by the German Research Foundation (Deutsche Forschungsgemeinschaft, DFG) in the framework of the research training group GRK 2462 “Processes in natural and technical Particle-Fluid-Systems” (PintPFS), which is gratefully acknowledged (Project No. 390794421).

Funding Open Access funding enabled and organized by Projekt DEAL.

Declarations

Conflict of interest The authors declare no conflict of interest. Boehringer Ingelheim GmbH & Co. KG is the new employer of M.D. and was not associated with this work.

Open Access This article is licensed under a Creative Commons Attribution 4.0 International License, which permits use, sharing, adaptation, distribution and reproduction in any medium or format, as long as you give appropriate credit to the original author(s) and the source, provide a link to the Creative Commons licence, and indicate if changes were made. The images or other third party material in this article are included in the article's Creative Commons licence, unless indicated otherwise in a credit line to the material. If material is not included in the article's Creative Commons licence and your intended use is not permitted by statutory regulation or exceeds the permitted use, you will need to obtain permission directly from the copyright holder. To view a copy of this licence, visit <http://creativecommons.org/licenses/by/4.0/>.

References

- International Maritime Organization. IMO (2022). <https://www.imo.org/> (visited on 04/20/2022)
- den Boon, H, Just H, Hansen PF, Ravn ES, Frouws JW, Otto S, Dalhoff P, Stein J, vd Tak C, van Rooij J (2004) Reduction of ship collision risks for offshore wind farms-safeship. In: EWEC 2004 proceedings. The European Wind Association EWEA, pp 1–9
- Ehlers S, Tabri K, Romanoff J, Varsta P (2012) Numerical and experimental investigation on the collision resistance of the X-core structure. *Ships Offshore Struct* 7(1):21–29
- Ringsberg J, Hogström P (2013) A methodology for comparison and assessment of three crashworthy side-shell structures: the X-core, Y-core and corrugation panel structures, pp 323–330
- Werner B, Daske C, Heyer H, Sander M, Schöttelndreyer M, Fricke W (2014) The influence of weld joints on the failure mechanism of scaled double hull structures under collision load in finite element simulations. In: *Procedia Materials Science* 3 (2014). 20th European conference on fracture, pp 307–312
- Yamada Y, Endo H, Pedersen P (2008) Effect of Buffer Bow Structure In Ship-Ship Collision. *Int J Offshore Polar Eng* 18:133–141
- Schöttelndreyer M (2015) Füllstoffe in der Konstruktion: Ein Konzept zur Verstärkung von Schiffsseitenhüllen". Ph.D. thesis. Technische Universität Hamburg
- Woitzik C, Chaudry M, Wriggers P, Düster A (2016) Experimental and numerical investigation of granular materials for an increase of the collision safety of double-hull vessels. *PAMM* 16:409–410
- Woitzik C, Düster A (2020) Experimental investigation of granules as crash-absorber in ship building. *Ships Offshore Struct* 16:314–325
- Woitzik C, Chaudry M, Wriggers P, Düster A (2018) Modelling and experimental testing of expanded granules as crash-absorber for double hull ships. *PAMM* 18:1–2
- Woitzik C, Düster A (2017) Modelling the material parameter distribution of expanded granules. *Granular Matter* 19(3):52
- Chaudry M, Woitzik C, Weißenfels C, Düster A, Wriggers P (2016) DEM-FEM coupled numerical investigation of granular materials to increase crashworthiness of double-hull vessels. *PAMM* 16(1):311–312
- Chaudry M, Woitzik C, Düster A, Wriggers P (2017) Experimental and numerical characterization of expanded glass granules. *Comput Part Mech* 152:106671
- Chaudry M, Woitzik C, Düster A, Wriggers P (2021) A multiscale DEM-FEM coupled approach for the investigation of granules as crash-absorber in ship building. *Comput Part Mech* 9:179–197
- Chaudry M, Wriggers P (2017) On the computational aspects of comminution in discrete element method. *Comput Part Mech* 5:1–15
- Potyondy DO, Cundall PA (2004) A bondedparticle model for rock. *Int J Rock Mech Min Sci* 41(8):1329–1364
- Simo JC, Hughes TJR (1998) *Computational inelasticity*. Interdisciplinary applied mathematics. Springer, New York
- Woitzik C (2021) Experimental testing and numerical simulation of granules as crash absorber for double hull structures. Ph.D. thesis. Technische Universität Hamburg
- Poraver. Poraver@ website (2022). <https://poraver.com/en/poraver/> (visited on 05/30/2022)
- Cundall PA, Strack ODL (1979) A discrete numerical model for granular assemblies. *Géotechnique* 29(1):47–65
- Dosta M, Skorych V (2020) MUSEN: an opensource framework for GPU-accelerated DEM simulations. *SoftwareX* 12:100618
- Wriggers P, Avci B (2020) Discrete element methods: basics and applications in engineering. In: De Lorenzis L, Düster A (eds) *Modeling in engineering using innovative numerical methods for solids and fluids*. Springer International Publishing, Berlin, pp 1–30
- Zhu HP, Zhou ZY, Yang RY, Yu AB (2007) Discrete particle simulation of particulate systems: theoretical developments. *Chem Eng Sci* 62(13):3378–3396
- Verlet L (1967) Computer “Experiments” on classical fluids. I. Thermodynamical properties of Lennard–Jones molecules. *Phys. Rev.* 159(1):98–103
- Quentrec B, Brot C (1973) New method for searching for neighbors in molecular dynamics computations. *J Comput Phys* 13(3):430–432
- Deresiewicz H, Mindlin RD (1952) Elastic spheres in contact under varying oblique forces. Department of Civil Engineering, Columbia University, New York
- Tsuji Y, Tanaka T, Ishida T (1992) Lagrangian numerical simulation of plug flow of cohesionless particles in a horizontal pipe. *Powder Technol* 71(3):239–250
- Young P (2013) The leapfrog method and other “symplectic” algorithms for integrating Newton’s laws of motion, pp 115/242
- Potyondy DO (2007) Simulating stress corrosion with a bonded-particle model for rock. *Int J Rock Mech Min Sci* 44(5):677–691
- Brown NJ, Chen J-F, Ooi JY (2014) A bond model for DEM simulation of cementitious materials and deformable structures. *Granul Matter* 16(1):299–311
- O’Sullivan C, Bray JD (2003) Selecting a suitable time step for discrete element simulations that use the central difference time integration scheme. *Eng Comput* 21(1):278–303
- Yousefi A, Ng T-T (2017) Dimensionless input parameters in discrete element modeling and assessment of scaling techniques. *Comput Geotech* 88:164–173
- Horabik J, Beczek M, Mazur R, Parafiniuk P, Ryżak M, Molenda M (2017) Determination of the restitution coefficient of seeds and coefficients of visco-elastic Hertz contact models for DEM simulations. *Biosyst Eng* 161:106–119. <https://doi.org/10.1016/j.biosystemseng.2017.06.009>
- Gross D, Hauger W, Schröder J, Wolfgang A. Wall (2013) In: De Lorenzis L, Düster A (eds) *Technische Mechanik 3: Kinetik*. Springer, Berlin
- Thölen AR (1992) Particle-particle interaction in granular material. In: Singer IL, Pollock HM (eds) *Fundamentals of friction: macroscopic and microscopic processes*. Springer, Dordrecht, pp 95–110. https://doi.org/10.1007/978-94-011-2811-7_6

Publisher’s Note Springer Nature remains neutral with regard to jurisdictional claims in published maps and institutional affiliations.